Minimizing the acoustic power radiated by a fluid-loaded curved panel excited by turbulent boundary layer flow

Micah R. Shepherd and Stephen A. Hambric

Citation: The Journal of the Acoustical Society of America **136**, 2575 (2014); doi: 10.1121/1.4896823
View online: https://doi.org/10.1121/1.4896823
View Table of Contents: https://asa.scitation.org/toc/jas/136/5
Published by the Acoustical Society of America

Minimizing the acoustic power radiated by a fluid-loaded curved panel excited by turbulent boundary layer flow

Micah R. Shepherd[a] and Stephen A. Hambric
Applied Research Laboratory, The Pennsylvania State University, P.O. Box 30, State College, Pennsylvania 16804

(Received 20 February 2014; revised 11 September 2014; accepted 19 September 2014)

In order to address noise control problems in the design stage, structural-acoustic optimization procedures can be used to find the optimal design for reduced noise or vibration. However, most structural-acoustic optimization procedures are not general enough to include both heavy fluid loading and complex forcing functions. Additionally, it can be difficult to determine and assess trade-offs between weight and sound radiation. A structural-acoustic optimization approach is presented for minimizing the radiated power of structures with heavy fluid loading excited by complex forcing functions. The procedure is demonstrated on a curved underwater panel excited by a point drive and by turbulent boundary layer flow. To facilitate more efficient analysis, an uncorrelated pressure assumption is made for the turbulent boundary layer forcing function. The thicknesses of groups of elements were used as the design variables with an adaptive covariance matrix evolutionary strategy as the search algorithm. The objective function was a weighted sum of total sound power and panel mass and the Pareto front was computed to show the optimum trade-off between the two objectives. The optimal designs are presented which illustrate the best methods for reducing radiated sound and mass simultaneously. © *2014 Acoustical Society of America*.
[http://dx.doi.org/10.1121/1.4896823]

PACS number(s): 43.40.Rj, 43.40.Dx [LH] Pages: 2575–2585

I. INTRODUCTION

Structural-acoustic optimization (SAO) procedures can be well suited to optimize a structure for low noise or other desired acoustic behavior. They can be especially useful for addressing noise or vibration criteria in the design stage. The optimization algorithm searches a structural-acoustic design space to locate the optimum set of design variables using either gradient information or evolutionary techniques. The reliability of the result depends on the fidelity of the structural-acoustic analysis and the robustness of the search algorithm.

A number of informative articles on SAO can be found in the literature over the last 25 yrs. The structures of interest have included simple beams/plates,[1–5] curved shells/cylinders,[6–9] sandwich structures,[9–13] musical instruments,[14,15] and various automotive/aerospace vehicle components.[16–19] Many of these works used analytical methods or finite element (FE)/boundary element (BE) analyses to compute the radiated pressure or power from single or multi-point harmonic excitation as the objective function to be reduced. Some included static pressure loads[5] or acoustic excitation of the structure such as monopole sources[9,12] or plane waves.[13,20] Due to the computation cost often associated with BE analysis, the number of design variables has typically been relatively low. A summary of the different objective functions, design variables, and constraints from these and other works is found in review articles by Marburg[21] and Marburg and Nolte.[22]

Relatively few articles have considered SAO with spatially-complex forcing functions particularly when heavy fluid loading was included. In many instances, spatially-complex or partially-correlated forcing functions are more realistic than the point drive, static pressure, or acoustic plane wave approaches which have been used in the literature. A few exceptions include Fahnline *et al*., who found the optimum metal alloy for a laser free-formed hydrofoil subjected to trailing edge flow forces,[23] and Grissom *et al.* who optimized the vibration absorber location for a pressure vessel excited by uncorrelated random pressures over the entire structure.[24] Joshi *et al*. optimized the location and curvature of ribs on a stiffened panel excited by a diffuse acoustic field[16] and turbulent boundary layer (TBL) flow.[25] In these papers, the frequency resolution was coarse in order to make the solution time tractable. However, the spacing between frequency bins was insufficient to adequately resolve the resonance peaks of the response, causing the true value of the response to be biased. In an effort to reduce the objective function, the optimizer pushed the response peaks in between frequency bins thus creating a bias in the objective function and therefore an artificial optimal design. Additionally, heavy fluid loading was not considered in their formulation.

It is desirable to develop a general SAO procedure which can include arbitrary forcing functions and heavy fluid loading so that TBL-induced noise of marine structures can be reduced. This paper presents such a procedure and demonstrates it on a curved underwater panel that is excited by a point drive and then by TBL flow at 10 knots. Since noise reduction often comes at the cost of increased mass, the optimization will be performed for the two-objective problem, where the weighted sum of the panel mass and radiated

[a]Author to whom correspondence should be addressed. Electronic mail: mrs30@psu.edu

sound power is reduced. The weighting coefficient is varied to estimate the Pareto optimality front which illustrates the competing nature of the two objectives and shows the optimal trade-off between designs. The optimization is first performed on the panel excited by a point drive to show proof of concept and illustrate the usefulness of the Pareto front. Results for the TBL-excited panel are then presented for a 9 design variable problem and a 98 design variable problem, where the design variables are defined as the thicknesses of groups of elements. The optimal reduction in sound power is achieved by a design which pushes the resonance peaks away from the peak in the TBL pressure spectrum. Finally, the results are compared for the three cases showing the general trends when more complexity is introduced into the optimization problem.

II. METHODS

A. Structural-acoustic analysis

To compute the vibration response of a driven structure in physical coordinates, one must solve the damped, forced equation of motion with a time-harmonic excitation

$$\boldsymbol{M}\ddot{x} + \boldsymbol{B}\dot{x} + \boldsymbol{K}x = Fe^{j\omega t}, \tag{1}$$

where $\boldsymbol{M}$, $\boldsymbol{B}$, and $\boldsymbol{K}$ are the mass, damping, and stiffness matrices, F is the force vector, and ω is the angular frequency. This is typically performed on a discretized structure using FE analysis. The velocity frequency response function (FRF) can be determined as

$$\boldsymbol{H}(\omega) = j\omega[-\omega^2\boldsymbol{M} + j\omega\boldsymbol{B} + \boldsymbol{K}]^{-1}. \tag{2}$$

Fluid-loading and complex impedance effects can also be included by adding their respective matrices to the denominator of the right hand side of Eq. (2). The computation of the added mass and damping caused by the fluid will be discussed subsequently.

Since the response can be recreated using a summation of normal modes, significant computational savings can be obtained by working in modal space as there are typically far fewer modes than physical points. The modal FRF equation can be obtained once the normal modes, denoted as ϕ, are known:

$$\boldsymbol{h}(\omega) = j\omega[-\omega^2\boldsymbol{m} + j\omega\boldsymbol{b} + \boldsymbol{k}]^{-1}. \tag{3}$$

In Eq. (3), $\boldsymbol{m} = \phi^T\boldsymbol{M}\phi$ is the modal mass, $\boldsymbol{b} = \phi^T\boldsymbol{B}\phi$ is the modal damping, and $\boldsymbol{k} = \phi^T\boldsymbol{K}\phi$ is the modal stiffness. When the mode shapes are mass-normalized, the modal mass matrix becomes the identity matrix and the modal stiffness matrix becomes a diagonal of eigenvectors, ω_n^2. The velocity response can therefore be computed in physical coordinates in terms of modes according to

$$V(\omega) = \boldsymbol{H}(\omega)F = [\phi\boldsymbol{h}(\omega)\phi^T]F = \phi h(\omega)f, \tag{4}$$

where $f = \phi^T F$ is the modal force vector.

For random analysis, spectral density quantities can be computed using the expected value

$$\boldsymbol{G}_{VV} = 2\lim_{T\to\infty}\frac{1}{T}E\left[V(\omega)V^H(\omega)\right], \tag{5}$$

where E is the expectation operator and T is a reference period. To accommodate these computations in modal coordinates, the modal forcing function cross-spectral density (CSD) matrix is defined as

$$G_{ff} = \phi^T G_{FF}\phi. \tag{6}$$

G_{FF} can be any stochastic excitation that is stationary and ergodic so that G_{ff} describes the coupling between any matrix of external forces and the vibration modes. More generally, Eq. (6) represents the modal acceptance of energy matrix and can be rewritten in the form

$$G_{ff} = \int\int_S \phi_i\phi_j G_{FF}dS, \tag{7}$$

which resembles the joint acceptance function.[26]

The modal amplitudes caused by the forcing function can now be computed to form a modal response CSD matrix

$$\boldsymbol{G}_{\psi\psi} = \boldsymbol{h}(\omega)G_{ff}\boldsymbol{h}(\omega)^H. \tag{8}$$

This is the modal equivalent of the multiple input multiple output problem (in matrix form) found in Bendat and Piersol.[27] The velocity response matrix can now be defined in terms of $\boldsymbol{G}_{\psi\psi}$ as

$$\boldsymbol{G}_{VV} = \phi\boldsymbol{G}_{\psi\psi}\phi^H. \tag{9}$$

The radiated sound power spectral density can be computed, given the resistance matrix R is known, using

$$G_{P_{\text{rad}}} = \sum_{m=1}^{M}\sum_{n=1}^{M} r_{mn}\boldsymbol{G}_{\psi_m\psi_n}, \tag{10}$$

where $r_{mn} = \phi_m^T R\phi_n$ is the modal resistance matrix and M is the number of retained modes. This analysis procedure has been used to predict TBL-induced acoustic power sources in elbowed pipes.[28] The modal resistance matrix can be computed using analytical formulations for simple cases or using BE methods.

For this work, the fluid loading effects were determined by estimating the fluid impedance matrix $Z(\omega) = R(\omega) + jX(\omega)$ using BEs. A lumped parameter BE method was used to determine the surface pressure given a unit volume velocity of each BE.[29] The resulting fluid forces, which completely characterize the additional mass and damping from the fluid,[30] were then converted to have units of dynamic stiffness, transformed to modal space and incorporated directly into Eq. (3).[31]

$$\boldsymbol{h}(\omega) = j\omega[-\omega^2\boldsymbol{m} + j\omega\boldsymbol{b} + \boldsymbol{k} - j\omega\boldsymbol{r}(\omega) - \omega\boldsymbol{x}(\omega)]^{-1}. \tag{11}$$

The variables $\boldsymbol{r}$ and $\boldsymbol{x}$ are the modal resistance and reactance matrices of the fluid, respectively. By including the fluid-loading matrices directly into the modal transfer function

$\boldsymbol{h}(\omega)$, the *in vacuo* modes can still be used as the basis set for the analysis, an idea which was first introduced by Lax.[32]

During the optimization, the acoustic matrices were assumed to not vary significantly since the base structure thickness changes are small compared to the wavelengths of interest.[33] This results in significantly-reduced computational times since the matrices are only computed once and stored.[23,34] The only computation required is a matrix pre- and post-multiplication to transform R into modal space. The application of this concept to SAO is detailed more fully in Marburg *et al.*[5]

The analysis procedure outlined above computes the structural-acoustic response at discrete frequencies. Therefore, the total analysis time depends on the total number of frequencies evaluated. Since the frequency resolution required to resolve a resonance peak depends on its quality factor, $Q = f/\Delta f$, higher-frequency peaks with the same damping level will require a coarser frequency array to achieve the same resolution. To minimize the number of evaluation frequencies without compromising the resolution, the spacing between evaluation frequencies $\tilde{df}$ was determined using the previous evaluation frequency and the damping loss factor ($\eta = 1/Q$):

$$\tilde{df} = \frac{f_0 \eta}{N-1}, \tag{12}$$

where f_0 is the previous evaluation frequency and N is the desired number of points within a half-power band if a resonance peak were to exist at f_0. This is a special case of a logarithmic frequency array that will resolve all resonance peaks with approximately N points while reducing the total number of evaluation frequencies and total computation time.

B. Turbulent boundary layer forcing function

The forcing function matrix for turbulence-induced wall pressures resulting from flow over a structure can be computed using the product of a pressure auto-spectrum (φ) and a pressure cross-spectrum function (Γ),

$$G_{FF} = \varphi(\omega)\Gamma(\vec{r}, \omega). \tag{13}$$

The point pressure spectrum φ sets the amplitude of the force and depends on the flow conditions. The pressure spectrum used in the research was a modified version of the Chase model[35] defined as

$$\varphi(\omega) = \frac{3\rho^2 u_\tau^4}{f^*}\left[\frac{(f/f^*)^2}{\left\{(f/f^*)^2 + \hat{\alpha}^2\right\}^{3/2}}\right] e^{-14 f\nu/u_\tau^2}, \tag{14}$$

where f is the frequency, $f^* = U/2/\pi/\delta^*$ and all other variables are defined in Table I. Figure 1 shows the frequency dependence of the spectrum for flow at 10 knots. The peak in the spectrum occurs at 61.5 Hz.

The cross-spectrum Γ defines the partially-correlated regions of pressure over the structure and is often referred to as a coherence function. A well-known TBL coherence function model was proposed by Corcos[36] as

$$\Gamma(\xi_1, \xi_2, \omega) = e^{-\beta_1|\omega\xi_1/U_c|} e^{-\beta_2|\omega\xi_2/U_c|} e^{j\omega\xi_1/U_c}, \tag{15}$$

where ξ is the separation distance (the streamwise direction denoted with subscript 1 and spanwise with subscript 2) between points x_μ and x_ν, β is the decay constant (streamwise and spanwise), and U_c is the convective flow velocity. Although the Corcos model is often used in the literature due to its relative simplicity, it has been shown to overpredict low-wavenumber energy.[37] To correct this, Mellen[37] suggested the following TBL model:

$$\Gamma(\xi_1, \xi_2, \omega) = e^{-\sqrt{(\beta_1|\omega\xi_1/U_c|)^2 + (\beta_2|\omega\xi_2/U_c|)^2}} e^{j\omega\xi_1/U_c}. \tag{16}$$

The Corcos and Mellen models are compared in Fig. 2.

When the correlation length $L_c = U_c/\omega/\beta$ of the TBL pressure fluctuations is much less than unity, there is essentially no correlation between each point. This is mathematically written as a series of delta functions populating the coherence matrix and is analogous to a spatially random (rain-on-the-roof) excitation. The correlation length can be much less than unity at either high frequencies or low convective speeds, making the uncorrelated approximation valid with many underwater vehicles.

When computing the modal force [Eq. (6)], the spatially random excitation is approximately achieved when the structural wavelength is large compared to the L_c. This is equivalent to $k_c \gg k_b$ where $k_c = U_c/\omega$ is the convective

TABLE I. TBL flow parameters.

Density (ρ)	1000 kg/m^3
Friction velocity (u_τ)	0.1542 m/s
Free-stream velocity (U)	5.14 m/s (10 knots)
Convective velocity (U_c)	3.598 m/s
Boundary layer disp thickness (δ^*)	0.0022 m
Kinematic viscosity (ν)	1.15×10^{-6}
Stream-wise decay constant (β_1)	0.11
Span-wise decay constant (β_2)	0.7
Turbulence constant ($\hat{\alpha}$)	0.12

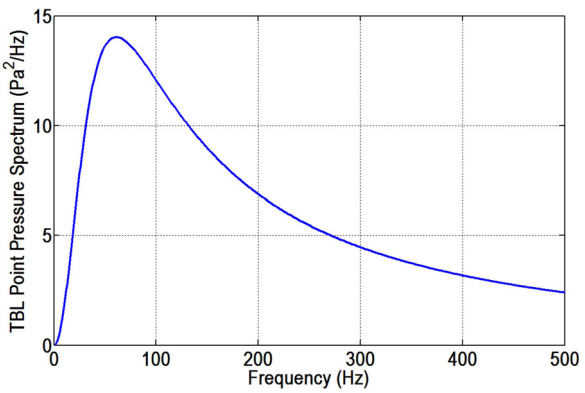

FIG. 1. (Color online) The point pressure spectrum (modified Chase model) using flow parameters found in Table I.

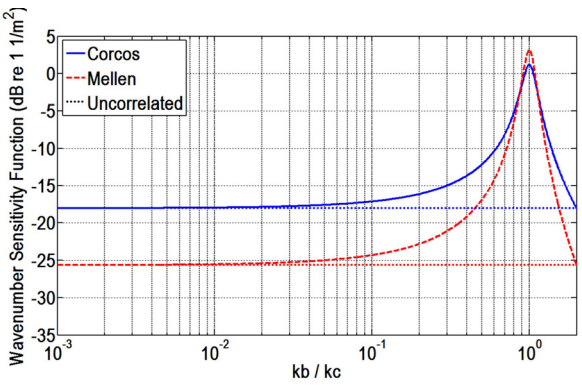

FIG. 2. (Color online) The Corcos (solid line) and Mellen (dashed line) sensitivity function (wavenumber spectrum) can be approximated by uncorrelated pressures (dotted line) at low wavenumbers.

wavenumber and k_b is the structural wavenumber. Since G_{ff} is modal-based, k_b will be the modal wavenumber and is therefore fixed in frequency and wave speed. Once the uncorrelated assumption has been satisfied for a single mode, it will also hold for all higher order modes since the convective wavenumber has a one over frequency dependence while the bending wavenumber has a one over square root of frequency dependence.

Ichchou *et al.*[38] show that in the uncorrelated realm, the integration of the forcing function and the mode shapes become independent and can be computed separately. Furthermore, in the high frequency limit, the spatial integral of Eq. (16) is

$$\int_{-\infty}^{\infty}\int_{-\infty}^{\infty}\Gamma(\xi_1,\xi_2,\omega)d\xi_1 d\xi_2 = \frac{\pi}{2}\left(\frac{\beta_1^3}{(1+\beta_1^2)^{3/2}}\right)\left(\frac{2Uc}{\beta_1\omega}\right)\left(\frac{2Uc}{\beta_2\omega}\right). \quad (17)$$

The integration limits can be taken to infinity since the correlation lengths are very small. Equation (17) is similar to the low-wavenumber approximation by Hambric *et al.*[39] and exactly equivalent to the $k=0$ form of the wavenumber sensitivity function. Figure 2 shows the wavenumber sensitivity function of the Corcos and Mellen coherence model. The low wavenumber region is mostly independent of wavenumber and matches the uncorrelated approximation within 1 dB below $k_b/k_c = 1/7 \approx 0.143$ (see Fig. 2). This approximation also bypasses the requirement to overly refine the FE model in order to resolve the TBL fluctuations.[40]

C. Adaptive covariance matrix evolutionary strategy

Many of the papers dealing with SAO have used gradient-based optimization algorithms. Gradient-based methods require either explicit or approximate design variable sensitivity analysis to determine the derivative of the objective with respect to the design variables. While gradient-based algorithms can be very efficient on linear, convex, and unimodal problems, they typically do not perform well on discontinuous, multi-modal, or noisy objective functions. Evolutionary or stochastic algorithms on the other hand often perform well on highly complex or discontinuous functions, but usually at the cost of a large number of function evaluations. Evolutionary algorithms use random search and competition to mimic natural processes such as mating, mutation, and selection and evolve a population over a series of generation. By using probabilistic transition rules to guide the search, they can escape local optima and have a better global performance than gradient methods. For most mid- to large-sized optimization problems, many function evaluations are often required for the algorithm to search the space, though typically much fewer than if a random or exhaustive search had been used.

When performing optimization, the objective function must be defined as a scalar. For optimization problems where the objective function varies with frequency, such as many structural-acoustic problems, F_{obj} must be cast into a scalar form using integration or some other averaging. Butkewitsch and Steffen investigated frequency response optimization using a combined objective-constraint approach to minimize the maximum of the FRF and discovered that the maximum value of a frequency response can be highly discontinuous over the design space.[41] Since gradient-based methods usually have difficulty with discontinuous search spaces, stochastic methods are often more appropriate for SAO when frequency-based objective functions are used.

The optimization algorithm that was used for this research was a real-valued evolutionary strategy with covariance matrix adaption (CMA-ES) developed by Hansen.[42] The algorithm adapts the covariance matrix of a proposed set of solutions to favor the solutions with the best fitness value. Figure 3 shows a graphical representation of the sampling procedure for a two design variable problem. The

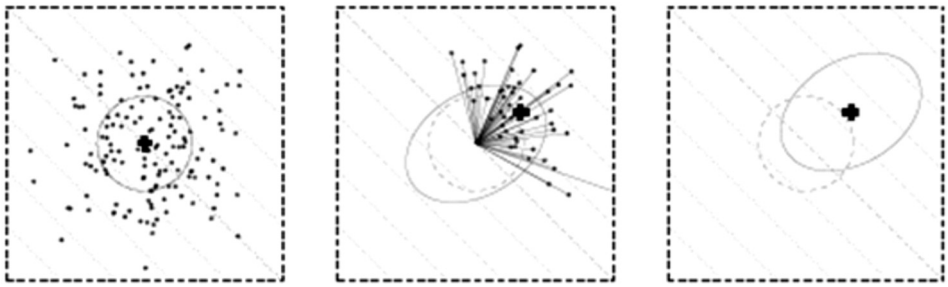

FIG. 3. The sampling and covariance matrix adaption of the CMA-ES algorithm as printed in Hansen (Ref. 43). An initial distribution is assumed and a series of samples are taken randomly from the distribution and evaluated (left). The points with the best fitness are used to estimate the new covariance matrix based on the distance from the initial mean (middle). A new mean is computed and the next generation covariance matrix is created (right).

TABLE II. Dimensions and material properties of the curved panel.

Streamwise length	2.086 m
Spanwise length	0.8 m
Radius of curvature	9.96 m
Modal loss factor	0.02
Young's modulus	195 GPa
Density	7700 kg/m^3
Poisson's ratio	0.28

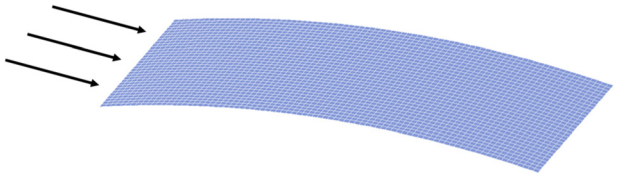

FIG. 4. (Color online) FE mesh of the curved panel. The arrows indicate the direction of the flow. The short edges were simply supported and the long edges were free.

covariance matrix is initially populated with a defined number of candidate solutions which are distributed about a mean value. This distribution is then adapted based on the fitness of each solution and their respective distance from the mean. New candidate solutions are sampled according to the multivariant distribution and the process is repeated until a stop criterion is reached. For a convex-quadratic function, the covariance matrix will adaptively estimate the inverse Hessian matrix and thus is similar to the quasi-Newton gradient-based method.[43] However, the design space is not confined to any particular geometrical condition (i.e., convex or concave). CMA-ES is also known to have several invariance properties which make it superior to many other stochastic optimization algorithms.[42]

III. CURVED PANEL OPTIMIZATION

The curved panel optimized in this paper is a notional representation of a panel from a marine vehicle. A FE model was created using 2688 linear shell elements with material properties of steel (see Table II). The panel was approximately 2.1 m × 0.8 m with 84 elements in the long direction and 32 elements in the short direction and an approximate element area of 6.2×10^{-4} m. Element thickness was used as the design variables during the optimization. The shorter edges are both simply supported while the longer edges are unconstrained and the panel curvature is approximately 6° along the center. The flow direction is along the length of the panel as shown in Fig. 4. The first six mode shapes and natural frequencies of the panel with thickness of 31.8 mm are shown in Fig. 5.

The optimization problem is stated formally as

$$\textbf{min:}\ F_{\text{obj}}, \tag{18}$$

$$\textbf{subject to:}\ \vec{x}^L \le \vec{x} \le \vec{x}^U,$$

where $\vec{x}$ is the vector of design variables and the superscripts L and U indicate lower and upper bounds, respectively. The objective function F_{obj} is a weighted sum of the total radiated sound power (P_{tot}) (Ref. 44) and the panel mass w, where each objective is normalized by its initial value, as denoted by the subscript 0,

$$F_{\text{obj}} = \alpha\left(\frac{P_{\text{tot}}}{P_0}\right) + (1-\alpha)\left(\frac{w}{w_0}\right). \tag{19}$$

The weighting coefficient α was varied between 0 and 1 to determine a Pareto front.[45]

Since the total radiated sound power was computed with non-uniform frequency spacing, P_{tot} was computed according to

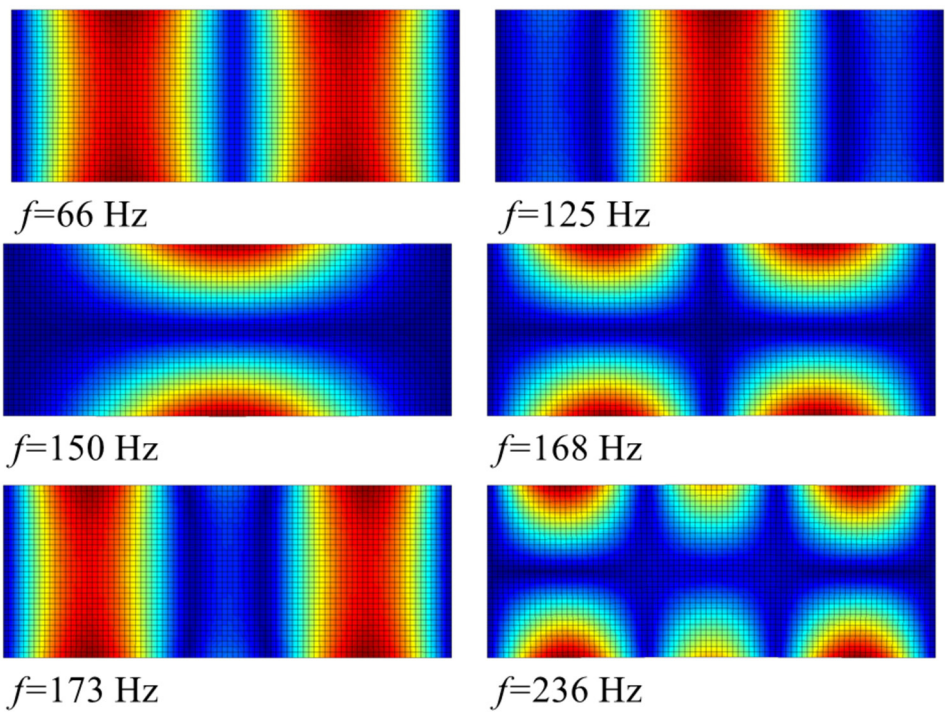

FIG. 5. (Color online) The mode shapes and natural frequencies of the curved panel with isotropic thickness of 31.8 mm (top view). The lighter shades indicate large deflection (positive or negative) while the darker shades represent no motion.

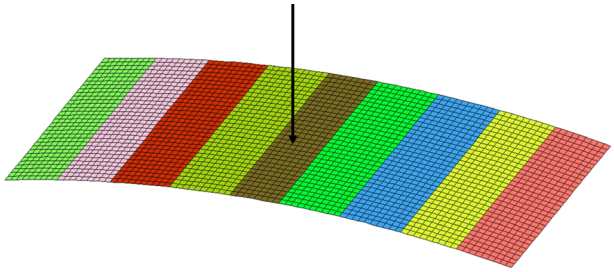

FIG. 6. (Color online) FE mesh of the curved panel with the thicknesses of nine strips of elements used as the design variables (distinguished by different shades). The location of the point drive is shown as an arrow. Optimization was performed with a point drive and with TBL excitation.

$$P_{\text{tot}} = \sum_i P_i df_i. \tag{20}$$

The analysis frequency was set from 10 to 500 Hz with the first 50 modes used in the modal summation. The natural frequency of highest-order mode was verified for the lowest thickness cases to be at least 1.5 times the highest analysis frequency.

Three optimization cases were performed. For the first case, nine strips of elements were grouped together and the thickness of each group was used as the design variable. The thickness was initially set to 31.8 mm and varied from between 12.7 and 50.8 mm. The panel is shown in Fig. 6 with the strips shown in separate colors. The panel was excited with a point drive in the center of the panel, oriented in the normal direction (indicated by the arrow in Fig. 6). The initial covariance matrix was set to have a standard deviation of 0.007 so that the initial distribution encompassed the range of the possible thicknesses. The radiated sound power for the point drive panel is shown in Fig. 7.

In the second case, the panel was excited by TBL flow at 10 knots. The flow speed is sufficiently slow enough so that the uncorrelated pressure approximation was used (see Sec. II B). The Mellen cross-spectrum model was used with the modified Chase point pressure spectrum, with flow parameters as listed in Table I.

The final optimization case was also excited by TBL at 10 knots but with the thickness of 98 patches of elements as the design variables (see Fig. 8). The element groups were 5

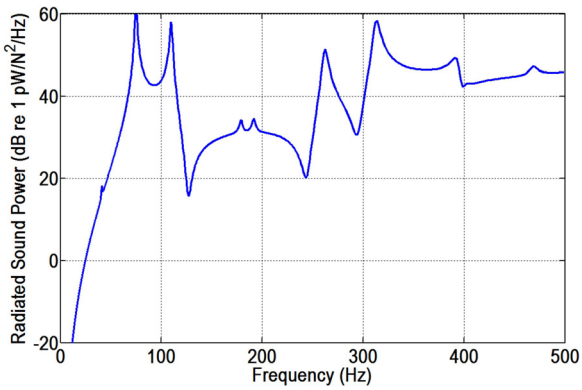

FIG. 7. (Color online) Radiated sound power for the point-driven panel with uniform thickness.

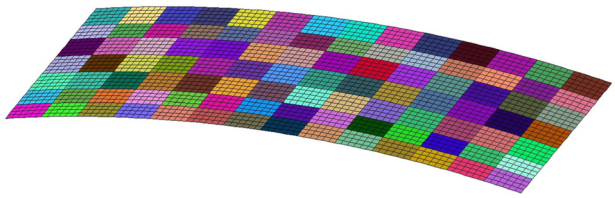

FIG. 8. (Color online) FE mesh of the curved panel with the thicknesses of 98 patches of elements used as the design variables (distinguished by different shades). Optimization was performed for TBL excitation at 10 knots.

elements wide and 6 elements long with 7 groups along the width of the panel and 14 along the length. Three rows of element groups were only four elements wide.

The population size was initially set at $4 + floor(3 \ln N)$, where N is the number of design variables, as recommended by Hansen.[43] The optimization was then repeated with double the population size to diversify the search. Since the initial design variables are chosen at random, this provides stronger evidence that a local minimum was not found. When the results were not identical, the more optimal of the two runs was used in the Pareto curve. If the two results were greater than 5% different, one of the runs was repeated. The optimizer stop criterion for all three cases was defined by a minimum objective change or maximum number of function evaluations. The number of function evaluations was determined using run-time estimates and available compute time. To ensure the optimizer had converged to a solution, the objective function was compared to previous generations. The run parameters for the three cases are listed in Table III.

A. Case I: Point drive with nine design variables

The optimization was first performed on the curved panel with a point excitation. The radiated sound power for several values of the weighting coefficient α is shown in Fig. 9. When $\alpha = 1.0$, only radiated sound is used to compute F_{obj} and therefore the lowest radiation is achieved. However, significant reduction is also achieved for $\alpha = 0.75$. The lowest reduction is found when $\alpha = 0$ since only the mass is used to determine F_{obj}. The total sound power levels are shown in Table IV.

The Pareto optimality front estimate is shown in Fig. 10 and illustrates the competing nature of the two objective functions. When $\alpha = 1$, the objective function minimizes only the radiated sound power (the right end of the curve) at the cost of increasing weight. When $\alpha = 0$, the objective function minimizes only the weight (the left end of the curve) at the cost of increasing the radiated sound power. The total difference in weight between the two ends of the Pareto front is 194.8 kg while the difference in radiated

TABLE III. The number of design variables, population size, and stop criterion (number of evaluations) for the three different optimization cases.

Case	Excitation	Design variables ($\vec{x}$)	Population size	# Evaluations
1	Point drive	9	10/20	1500/2500
2	TBL	9	10/20	1500/2500
3	TBL	98	17/34	4000/5500

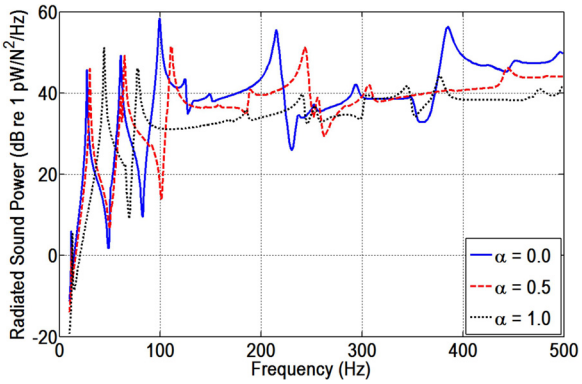

FIG. 9. (Color online) Radiated sound power for the curved panel with a point drive and nine design variables, where $\alpha = 1.0$ corresponds to reducing radiated sound only and $\alpha = 0$ corresponds to reducing mass only.

sound is 8.2 dB. For weighting coefficients between zero and one, the two objectives are considered simultaneously and the Pareto front shows the ideal trade-off conditions for reducing both.

Table IV shows the values used to build the Pareto front for each value of α. The value objective function is also shown. The maximal trade-off between the two objectives is found at the "knee" region of the front when $\alpha = 0.5$. The knee represents the solution with the most reduction in both weight and sound power. To the right of the knee, the objective is more sensitive to weight and significant reduction in weight can be achieved with relatively low increase in radiated sound. To the left of the knee, it is more sensitive to radiated sound power and significant reduction can be achieved with relatively low increase in weight.

The optimized thickness distributions for case I are shown in Fig. 11. The $\alpha = 0.0$ case found the smallest thickness (1.27 mm) for each strip to achieve the lowest mass, as expected. The $\alpha = 1.0$ case on the other hand, only considers the radiated power so that the panel was thickened on the strip where the drive is located. The two strips surrounding this strip were also thickened even more than the center panel to create an impedance mismatch to partially isolate the input energy. The cases for $\alpha = 0.0 - 1.0$ show the center strip and side strips thickening gradually to balance reducing sound and mass. The thickness of the first strip of elements is also gradually increased as α increased.

Although these optimization results can be confirmed intuitively, figuring out the balance between mass and sound can be very difficult to determine without the aid of a global

TABLE IV. Optimized results for the point-drive panel with nine design variables for each weighting coefficient. $\alpha = 1.0$ corresponds to reducing radiated sound only and $\alpha = 0$ corresponds to reducing mass only.

α	Power (dB re 1 pW)	Weight (kg)	F_{obj}	ΔdB	Δw
0.0	72.2	164.4	0.399	−1.13	−247.2
0.125	70.1	172.5	0.426	−3.26	−239.1
0.25	68.2	187.2	0.417	−5.16	−224.4
0.5	67.7	195.6	0.373	−5.67	−215.9
0.625	66.9	214.2	0.339	−6.37	−197.4
0.75	64.4	326.1	0.295	−8.87	−85.4
1.0	64.0	359.2	0.118	−9.28	−52.3

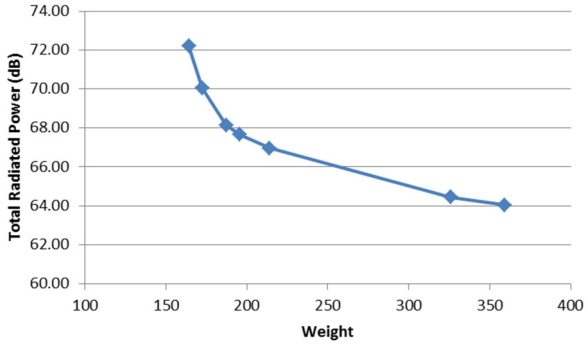

FIG. 10. (Color online) The Pareto front for the curved panel with a point excitation. The knee is located at $\alpha = 0.5$. Weight is shown in kilograms.

optimizer. Additionally, the information in the Pareto front can be very valuable for decision making. For example, the relative benefit of reducing sound can be easily related to the cost of added mass. Alternatively, the panel can be designed for the lowest sound radiation given an absolute mass constraint or vice versa.

B. Case II: TBL excitation with nine design variables

Optimization was then performed on the curved panel excited by TBL flow at 10 knots. The Pareto front for this

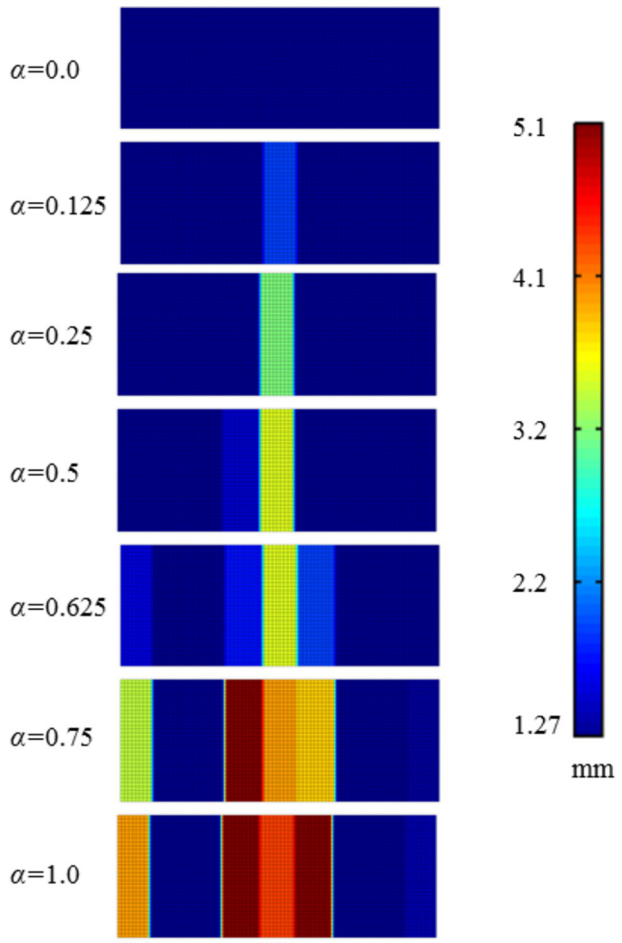

FIG. 11. (Color online) Thickness distribution of the optimum curved panels excited by a point drive for each weighting coefficient, where $\alpha = 1.0$ corresponds to reducing radiated sound only and $\alpha = 0$ corresponds to reducing mass only.

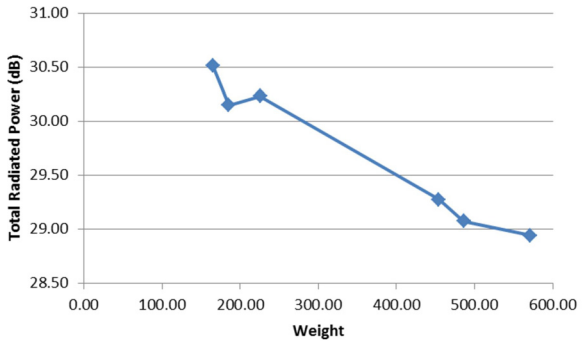

FIG. 12. (Color online) The Pareto front for the curved panel with TBL excitation with weight shown in kilograms.

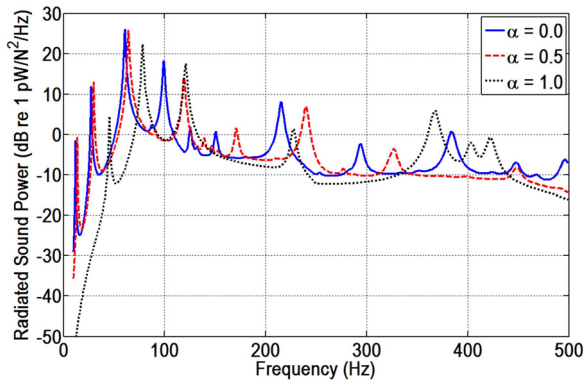

FIG. 13. (Color online) Radiated sound power for the curved panel with TBL excitation and nine design variables, where $\alpha = 1.0$ corresponds to reducing radiated sound only and $\alpha = 0$ corresponds to reducing mass only.

case is shown in Fig. 12, again showing the competing nature of the two objective functions. The total reduction in radiated sound power between the two extremes is only about 1.5 dB while the cost in weight is about 475 kg. This indicates a much higher sensitivity to weight than to radiated sound. The curve also indicates that the design space is difficult to search since it does not follow a smooth concave function.

Table V shows the values used to build the Pareto front. The objective function is reduced less than in case I indicating that it is more difficult to reduce noise on the TBL-excited panel than on a point drive panel.

The radiated sound power for case II is shown in Fig. 13. The sound power has peaks between 60 and 72 Hz for all cases and tails off at low and high frequencies, corresponding to the maximum in the point pressure spectrum φ. The reduction in sound power is achieved by moving the panel resonances away from the frequency of maximum TBL energy, which occurs at 61.5 Hz, the peak in the point pressure spectrum (see Fig. 1).

The associated thickness distributions are shown in Fig. 14. Again the $\alpha = 0.0$ case finds the smallest thickness for each strip. The $\alpha = 1.0$ case shifts the peaks upward and thickened strips to their maximum allowed value (except on the edge strips). The runs between 0.0 and 1.0 show a symmetric pattern alternating thick and thin strips. The alternating structure shows that impedance mismatching is a good way to reduce noise and save weight simultaneously.

The cause of the relatively small reduction in sound power was then considered. The radiated power can be reduced by either reducing the acceptance of energy (i.e., lowering the modal forcing function matrix) or reducing the efficiency of the radiation. The modal forcing function for the first mode is shown in Fig. 15 and is lowest when $\alpha = 1.0$. Since the modes are mass-normalized, the higher modal mass causes the lower acceptance of energy and therefore lower sound radiation. This trend is followed by all modes. The modal resistance matrix, on the other hand, does

TABLE V. Optimization results for the TBL-excited panel with nine design variables for each weighting coefficient. $\alpha = 1.0$ corresponds to reducing radiated sound only and $\alpha = 0$ corresponds to reducing mass only.

α	Power (dB re 1 pW)	Weight (kg)	F_{obj}	ΔdB	Δw
0.0	30.5	164.4	0.399	0.18	−247.2
0.25	30.5	164.7	0.560	0.16	−246.8
0.5	30.2	185.6	0.703	−0.2	−225.9
0.56	30.2	225.6	0.786	−0.12	−185.9
0.625	29.3	454.3	0.902	−1.08	42.7
0.75	29.1	486.1	0.854	−1.28	74.5
1.0	28.9	571.4	0.723	−1.41	159.8

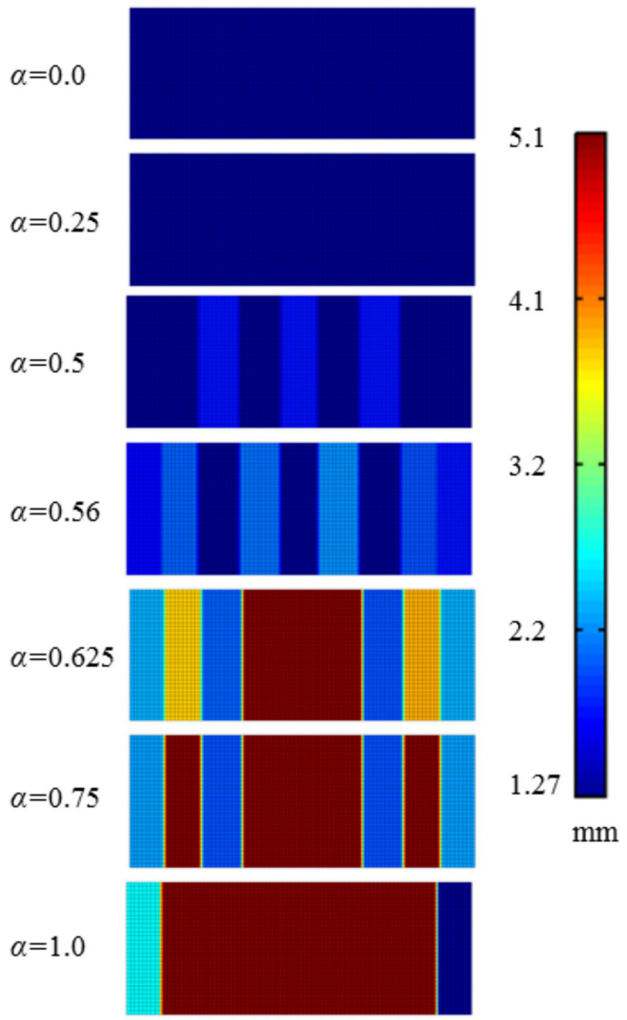

FIG. 14. (Color online) Thickness of the optimum curved panels excited by TBL for each case of α.

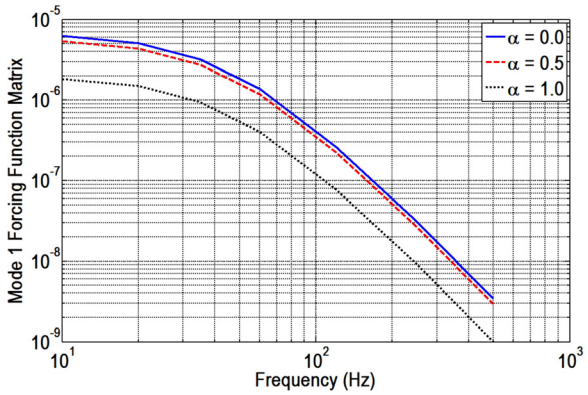

FIG. 15. (Color online) Modal forcing function for the first mode of optimal designs from several different weighting coefficients. The lower values indicate a lower acceptance of energy.

not follow any regular trends meaning that some modes radiate better for the $\alpha = 0.0$ case while others radiate better for the $\alpha = 1.0$ case. The overall effect is that the modal radiation efficiency does not change significantly during the optimization. This is consistent with the assumption that the radiation resistance does not change from design to design.

C. Case III: TBL excitation with 98 design variables

As a final case, optimization was performed on the TBL-excited curved panel with the thickness of 98 patches as the design variables. The radiated sound power is shown in Fig. 16 with the same trends as seen in case II. The resonance peaks in the radiated sound minimization are pushed away from the 61.5 Hz peak in the TBL energy. The optimized thickness distributions are shown in Fig. 17. Since there are many more possible design variables, the patterns are more complex. The trend seems to show a pattern which resembles a V-shape as α increases where the middle of the panel is thickened on one side with additional thickening on the opposite corners.

The Pareto front for this case is shown in Fig. 18, again showing the competing nature of the two objective functions. The total reduction in radiated sound power is only about 1.8 dB while the cost in weight is about 310 kg. Table VI shows the values used to build the Pareto front. In general,

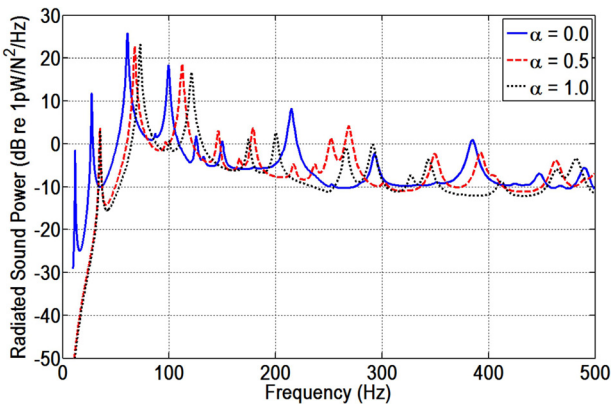

FIG. 16. (Color online) Radiated sound power for the curved panel with TBL excitation and 98 design variables, where $\alpha = 1.0$ corresponds to reducing radiated sound only and $\alpha = 0$ corresponds to reducing mass only.

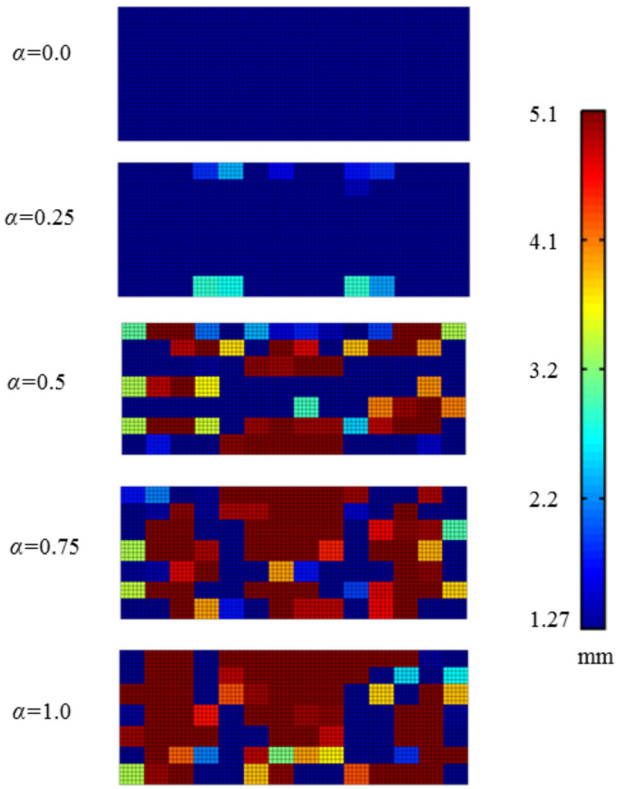

FIG. 17. (Color online) Thickness of the optimum curved panels excited by TBL for each case of α.

the objective functions are reduced more for the case with 98 patches than for the case with 9 strips. This is likely due to the greater diversity of possible designs when using smaller patches in both x and y directions.

D. Effect of increasing complexity on optimization results

The complexity of the optimization problem was increased between cases I–II and II–III. When transitioning from a point drive to a TBL forcing function, the optimizer basically performed the same. There seemed to be little difference in the approximate number of functions evaluation required to converge to a solution. It is reasonable to assume from this, that the optimizer is "blind" to the difficulty of the analysis required to compute the objective function. However, the increased complexity created a more difficult

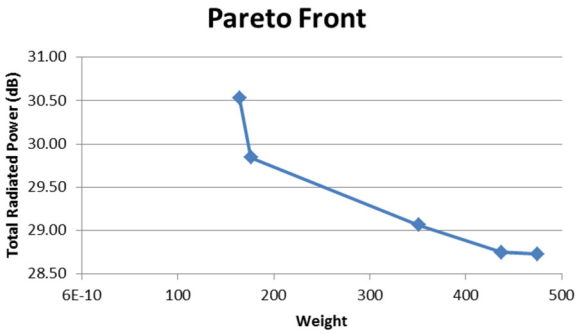

FIG. 18. (Color online) The Pareto front for the curved panel with TBL excitation and 98 design patches with weight shown in kilograms.

TABLE VI. Optimization results for the TBL-excited panel with 98 design variables for each weighting coefficient. $\alpha = 1.0$ corresponds to reducing radiated sound only and $\alpha = 0$ corresponds to reducing mass only.

α	Power (dB re 1 pW)	Weight (kg)	F_{obj}	ΔdB	Δw
0.0	30.5	164.4	0.399	0.18	−247.2
0.25	29.85	176.3	0.544	−0.51	−235.2
0.5	29.06	351.0	0.798	−1.29	−60.6
0.75	28.75	437.2	0.784	−1.61	25.6
1.0	28.73	474.3	0.688	−1.62	62.7

search space where little sound reduction could be achieved. A similar result was reported by Marburg *et al*. when comparing the radiated noise minimized by a point-driven and static pressure-loaded beam.[5] This suggests that the amount of noise reduction that can be achieved is due more to the spatially-extended nature of the drive, not the partial correlation.

Changing from 9 design variables to 98, however, did have an effect. More function evaluations were required when there are more design variables and therefore case III had a longer run time. However, the increase in the number of function evaluations does not scale linearly with increase in the number of design variables. Despite this benefit, the optimized design is much more difficult to visualize and interpret with a large number of design variables. Additionally, the optimized design is not likely to be directly usable and should be used mostly to learn trends and gain insight. For these reasons, a smaller number of design variables may be more useful for quick design evaluation.

IV. CONCLUSION

A general SAO procedure has been presented which can include spatially complex forcing functions and heavy fluid loading. Optimization was then performed on a curved underwater panel excited by a point drive and by TBL flow at 10 knots. The thicknesses of 9 strips/98 patches of elements were varied as the design variables and a weighted combination of radiated sound power and mass was minimized. Pareto fronts have been computed to show the relative sensitivity to reducing both simultaneously.

The results for the point-driven panel with nine design variables illustrate a gradual stiffening of the center strip at the location of the drive. The best radiated sound reduction comes from an impedance mismatch which isolates energy at the drive location. The Pareto front was computed to determine the trade-off between reducing noise and reducing mass.

For the TBL-excited panel, the reduction in radiated noise came from reducing the modal forcing function. This was achieved by pushing the resonance peaks away from the peak in the TBL energy. The optimal designs showed that alternating thin and thicker strips is the best way to reduce both weight and radiated sound for TBL excitation curved underwater panels. The case with 98 design variables showed a slightly greater reduction in radiated noise since the element thickness was varied in both the flow and cross-flow direction.

ACKNOWLEDGMENTS

M.R.S. gratefully acknowledges the financial support from Deborah Nalchajian of the Office of Naval Research.

[1]A. D. Belegundu, R. R. Salagame, and G. H. Koopmann, "A general optimization strategy for sound power minimization," Struct. Opt. **8**(2–3), 113–119 (1994).
[2]J. Y. Jeon and M. Okuma, "An optimum embossment of rectangular section in panel to minimize noise power," J. Vib. Acoust. **130**, 021012 (2008).
[3]K. Naghshineh, G. H. Koopmann, and A. D. Belegundu, "Material tailoring of structures to achieve a minimum radiation condition," J. Acoust. Soc. Am. **92**(2), 841–855 (1992).
[4]A. Ratle and A. Berry, "Use of genetic algorithms for the vibroacoustic optimization of a plate carrying point-masses," J. Acoust. Soc. Am. **104**(6), 3385–3397 (1998).
[5]S. Marburg, F. Dienerowitz, D. Fritze, and H. J. Hardtke, "Case studies on structural-acoustic optimization of a finite beam," Acta Acust. Acust. **92**(3), 427–439 (2006).
[6]E. W. Constans, G. H. Koopmann, and A. D. Belegundu, "The use of modal tailoring to minimize the radiated sound power of vibrating shells: Theory and experiment," J. Sound Vib. **217**(2), 335–350 (1998).
[7]K. A. Cunefare and B. S. Dater, "Structural acoustic optimization using the complex method," J. Comp. Acoust. **11**, 115–137 (2003).
[8]S. A. Hambric, "Sensitivity calculations for broad-band acoustic radiated noise design optimization problems," J. Vib. Acoust. **118**(7), 529–532 (1996).
[9]W. M. Johnson and K. A. Cunefare, "Use of principle velocity patterns in the analysis of structural acoustic optimization," J. Acoust. Soc. Am. **121**, 938–948 (2007).
[10]M. A. Lang and C. L. Dym, "Optimal acoustic design of sandwich panels," J. Acoust. Soc. Am. **57**(6), 1481–1487 (1975).
[11]F. Franco, K. A. Cunefare, and M. Ruzzene, "Structural-acoustic optimization of sandwich panels," J. Vib. Acoust. **129**, 330–340 (2007).
[12]H. Denli and J. Q. Sun, "Structural-acoustic optimization of sandwich structures with cellular cores for minimum sound radiation," J. Sound Vib. **301**, 93–105 (2007).
[13]H. Denli and J. Q. Sun, "Structural-acoustic optimization of sandwich cylindrical shells for minimum interior sound transmission," J. Sound Vib. **316**, 32–49 (2008).
[14]Y. Yu, I. G. Jan, I. K. Kim, and B. M. Kwak, "Nodal line optimization and its application to violin top plate design," J. Sound Vib. **329**, 4785–4796 (2010).
[15]W. Kausel, "Optimization of brasswind instruments and its application in bore reconstruction," J. New Music Res. **30**, 69–82 (2001).
[16]P. Joshi, S. B. Mulani, W. C. H. Slemp, and R. K. Kapania, "Multiobjective vibroacoustic optimization of stiffened panels excited by acoustic diffuse field," in *Proceedings of the 52nd AIAA/ASME Structural Dynamics and Material Conference*, AIAA 2011-1750 (2012).
[17]J. Bös, "Numerical optimization of the thickness distribution of three-dimensional structures with respect to their structural acoustic properties," Struct. Multidisc. Opt. **32**(1), 12–30 (2006).
[18]S. Marburg, H. J. Hardtke, R. Schmidt, and D. Pawandenat, "An application of the concept of acoustic influence coefficients for the optimization of a vehicle roof," Eng. Anal. Bound. Elem. **20**(4), 305–310 (1997).
[19]E. Yuksel, G. Kamci, and I. Basdogan, "Vibro-acoustic design optimization study to improve the sound pressure level inside the passenger cabin," J. Vib. Acoust. **134**, 061017 (2012).
[20]M. H. Shojaeifard, R. Talebitooti, and A. Yadollahi, "Optimization of sound transmission through laminated composite cylindrical shells using a genetic algorithm," Mech. Compos. Mater. **47**(4), 481–494 (2011).
[21]S. Marburg, "Developments in structural-acoustic optimization for passive noise control," Arch. Comput. Meth. Eng. **9**(4), 291–370 (2002).
[22]S. Marburg and B. Nolte, *Computational Acoustics of Noise Propagation in Fluids—Finite and Boundary Element Methods* (Springer, Berlin, 2008), pp. 25–27.
[23]J. B. Fahnline, T. E. McDevitt, E. J. Whitney, and D. E. Capone, "Structural-acoustic tailoring of metal structures by laser free-forming," Noise Cont. Eng. J. **54**(2), 124–129 (2006).
[24]M. D. Grissom, A. D. Belegundu, A. Rangaswamy, and G. H. Koopmann, "Conjoint-analysis-based multiattribute optimization: Application in acoustical design," Struct. Multidisc. Opt. **31**, 8–16 (2006).

[25]P. Joshi, S. B. Mulani, W. C. H. Slemp, and R. K. Kapania, "Vibro-acoustic optimization of turbulent boundary excited panel with curvilinear stiffeners," J. Aircraft **49**(1), 52–65 (2012).
[26]A. Powell, "On the fatigue failure of structures due to vibrations excited by random pressure fields," J. Acoust. Soc. Am. **30**(12), 1130–1135 (1958).
[27]J. S. Bendat and A. G. Piersol, *Random Data* (Wiley, New York, 2000), p. 263.
[28]S. A. Hambric, D. A. Boger, J. B. Fahnline, and R. L. Campbell, "Structure- and fluid-borne acoustic power sources induced by turbulent flow in 90° piping elbows," J. Fluids Struct. **26**, 121–147 (2010).
[29]G. H. Koopmann and J. B. Fahnline, *Designing Quiet Structures: A Sound Power Minimization Approach* (Academic Press, San Diego, 1997), pp. 1–244.
[30]D. T. Wilton, "Acoustic radiation and scattering from elastic structures," Int. J. Numer. Meth. **13**, 123–138 (1978).
[31]J. B. Fahnline, "Computing fluid-coupled resonance frequencies, mode shapes, and damping loss factors using the singular value decomposition," J. Acoust. Soc. Am. **115**(4), 1474–1482 (2004).
[32]M. Lax, "The effect of radiation on the vibrations of a circular diaphragm," J. Acoust. Soc. Am. **16**, 5–13 (1944).
[33]C. Pal and I. Hagiwara, "Dynamic analysis of a coupled structural-acoustic problem. Simultaneous multi-modal reduction of vehicle interior noise level by combined optimization," Finite Elem. Anal. Design **14**, 225–234 (1993).
[34]M. R. Shepherd and S. A. Hambric, "An approach for Structural-acoustic optimization of ribbed panels using component mode synthesis," in *Proceedings of Internoise 2012/ASME NCAD*, IN12-592 (2012).
[35]P. D. Lysak, "Modeling the wall pressure spectrum in turbulent pipe flows," J. Fluids Eng. **128**, 216–222 (2006).
[36]G. M. Corcos, "Resolution of pressure in turbulence," J. Acoust. Soc. Am. **35**(2), 192–199 (1963).
[37]R. H. Mellen, "On modeling convective turbulence," J. Acoust. Soc. Am. **88**(6), 2891–2893 (1990).
[38]M. N. Ichchou, B. Hiverniau, and B. Troclet, "Equivalent rain on the roof loads for random spatially correlated excitations in the mid-high frequency range," J. Sound Vib. **322**, 926–940 (2009).
[39]S. A. Hambric, Y. F. Hwang, and W. K. Bonness, "Vibrations of plates with clamped and free edges excited by low-speed turbulent boundary layer flow," J. Fluids Struct. **19**, 93–110 (2004).
[40]C. Hong and K. K. Shin, "Modeling of wall pressure fluctuations for finite element structural analysis," J. Sound Vib. **329**, 1673–1685 (2010).
[41]S. Butkewitsch and V. Steffen, "A case study on frequency response optimization," Int. J. Solids Struct. **38**, 1737–1748 (2001).
[42]N. Hansen, "An analysis of mutative σ-self-adaptation on linear fitness functions," Evol. Comp. **14**(3), 255–275 (2006).
[43]N. Hansen, "The CMA evolutionary strategy: A tutorial," accessed online at https://www.lri.fr/∼hansen/cmatutorial.pdf (Last viewed February 21, 2014).
[44]A near-field energy quantity may be a more appropriate objective function if considering an aircraft fuselage with passengers near the radiating structure. However, the uncorrelated pressure approximation would not be valid since the vehicle travels much faster.
[45]A. D. Belegundu and T. R. Chandrupatla, *Optimization Concepts and Applications in Engineering* (Prentice Hall, Englewood Cliffs, NJ, 1999), pp. 372–38.